ACS Appl. Mater. Interfaces 2019, 11, 34, 30610–30620
https://doi.org/10.1021/acsami.9b10444

Doxorubicin-Loaded Thermoresponsive Superparamagnetic Nanocarriers for Controlled Drug Delivery and Magnetic Hyperthermia Applications

Zied Ferjaoui[1], Enaam Jamal Al Dine[1], Aigul Jandayeva[2,3], Lina Bezdetnaya[2,3], Crosby Soon Chang[1], Raphaël Schneider[4,] Fabrice Mutelet[4], Damien Mertz[5], Sylvie Begin[5], Fabienne Quilès[6], Eric Gaffet[1] and Halima Alem*[1]

[1]Université de Lorraine, CNRS, Institut Jean Lamour (UMR 7198), Campus Artem 2 allée André Guinier - BP 50840, F54011 Nancy Cedex, France

[2]CRAN UMR 7039, CNRS, Université de Lorraine, Vandœuvre-lès-Nancy, France

[3]Reserach Department, Institut de Cancérologie de Lorraine, 6 avenue de Bourgogne CS 30519 54519 Vandœuvre-lès-Nancy Cedex, France

[4]Laboratoire Réactions et Génie des Procédés, Université de Lorraine, CNRS, LRGP, F-54000 Nancy, France

[5]Université de Strasbourg, CNRS, Institut de Physique et Chimie des Matériaux de Strasbourg, UMR 7504 , F-67034 Strasbourg, France

[6]Université de Lorraine, CNRS, UMR 7564, Laboratoire de Chimie Physique et Microbiologie pour l'Environnement (LCPME), Université de Lorraine, Nancy, France

ABSTRACT

This study reports on the development of thermoresponsive core/shell magnetic nanoparticles (MNPs) based on an iron oxide core and a thermoresponsive copolymer shell composed of 2-(2-methoxy)ethyl methacrylate (MEO2MA) and oligo(ethylene glycol)methacrylate (OEGMA) moieties. These smart nano-objects combine the magnetic properties of the core and the drug carrier properties of the polymeric shell. Loading the anticancer drug doxorubicin (DOX) in the thermoresponsive MNPs via supramolecular interactions provides advanced features to the delivery of DOX with spatial and temporal controls. The so coated iron oxide MNPs exhibit superparamagnetic behavior with a saturation magnetization of around 30 emu g–1. Drug release experiments confirmed that only a small amount of DOX was released at room temperature, while almost 100% drug release was achieved after 52 h at 42 °C with Fe3−δO4@P(MEO2MA60OEGMA40), which grafted polymer chains displaying a low critical solution temperature of 41 °C. Moreover, the MNPs exhibit magnetic hyperthermia properties as shown by specific absorption rate measurements. Finally, the cytotoxicity of the core/shell MNPs toward human ovary cancer SKOV-3 cells was tested. The results showed that the polymer-capped MNPs exhibited almost no toxicity at concentrations up to 12 μg mL–1, whereas when loaded with DOX, an increase in cytotoxicity and a decrease of SKOV-3 cell viability were observed. From these results, we conclude that these smart superparamagnetic nanocarriers with stealth properties are able to deliver drugs to tumor and are promising for applications in multimodal cancer therapy.

KEYWORDS: core/shell MNPs, responsive nanomaterials, hyperthermia, drug delivery, SKOV-3 cells.

INTRODUCTION

Superparamagnetic iron oxide nanoparticles (SPIONS) are well known to display magnetization only when a magnetic field is applied[1,2]. Moreover, they can generate heat upon application of a local high frequency alternating magnetic field (HAMF)[1,3–7]. This is particularly interesting when considering cancer therapy since cancer cells hardly survive a heating to 45°C[8–10]. Indeed, over 42°C the natural enzymatic processes ensuring the cells to be alive are destroyed, and the cancer cells become very sensitive to temperature[11,12]. In regards to the magnetic hyperthermia property, the development of

SPIONs for cancer therapy using magnetic hyperthermia is an increasing research field. Furthermore, the use of these nanoobjects is also envisioned for imaging and theranostics. Many structures with efficient magnetic hyperthermia properties have been developed like iron oxide nanoparticles[13–16] and lanthanide doped NPs.[17] To targeted specific application, and ensure the stability of the SPIONs, the grafting of polymer macromolecules at the surface of polymeric SPIONS is appealing compared to small molecules since the final core/shell NPs can take advantages of the macromolecules physico-chemical properties in physiological media [18]. Hence, stimuli responsive polymer have been grafted at the surface of SPIONs, to ensure responsiveness, drug loading and release at physiological range[19,20]. Thermo-responsive polymers are indeed known to exhibit either an Upper Critical Solution Temperature (UCST) or a LCST[19,21–23]. When the UCST is reached upon heating, the polymers become hydrophilic, whereas the LCST is the temperature at which the polymer chains will shrink due to the release of water molecule from their backbone leading to a decrease of the volume and to their hydrophobicity[21]. Consequently, the use of thermoresponsive polymers displaying a LCST in a temperature range of 40–42°C is of high interest for the design of core/shell NPs for biomedical applications[19,23]. Below the targeted temperature, once the thermo-responsive macromolecules are covalently grafted at the surface of SPIONs, the NPs can trap a cancer drug by specific interactions whereas their hydrophilicity allows their good dispersion and circulation in the blood[24,25]. Upon heating locally at 40–42°C, the drug release could be triggered in a temporal controlled way[25,26].

For example, poly(N-isopropylacrylamide) (PNIPAM), which is the most commonly used thermally responsive polymers with LCST of 32 °C, was grafted at the surface of SPIONs via grafting-onto and grafting from process. However, the low LCST[27] and the cytotoxicity[28] of the PNIPAM prevent its use for further clinical applications. Furthermore, pH responsive polymer with cationic groups in their backbone, such as poly-((2-dimethyl amino)ethyl methacrylate) (PDMAEMA) were grafted at the surface of inorganic core/shell γ-Fe_2O_3@SiO_2 and loaded with high amount of DOX (essentially within the silica shell) and RohB and the pH dependent release of the drug was demonstrated[29]. Other example in the literature shows that PDMAEMA and other positively charged polymers such as polyethylenimine (PEI), and polyamidoamine (PAMAM) can be used as gene carriers for gene delivery applications with nucleic acids loaded via electrostatic adsorptions [4,18,22,30,31]. For more details, the reader can refer to the following detailed review[4,22,32]. Moreover, when considering further applications of MNPs, which involve their introduction in biological environments such as blood, interstitial fluid, or extracellular matrix (ECM), the rapid covering of their surfaces by various proteins (called protein corona) has to be considered.[17,33–38] This protein corona modify the particle surface energy, size, cellular uptake, biodistribution, and toxicity. To achieve NPs with stealth properties, in one hand, poly(ethylene glycol) (PEG) chains were grafted on their surface by the grafting-to process (the

grafting of pre-synthesized polymer chains) method[15,39,40]. In another hand, co-polymers based on 2-(2-methoxy) ethyl methacrylate (MEO_2MA) and oligo (ethylene glycol) methacrylate (OEGMA) moieties have shown interesting features compared to PEG. Indeed, besides being biocompatible and proteins repellent, these polymers are thermo-responsive and display a tunable LCST in the range of body temperature depending the ratio of monomers used[25,41,42].

In this work, we report then the development and the characterization of superparamagnetic and thermo-responsive core/shell NPs that can be used as drug delivery systems. We have investigated *in vitro* their use as drug carriers towards the human ovarian cancer cell line (SKOV-3 cells). These NPs are composed of $Fe_{3-\delta}O_4$ NPs coated with $P(MEO_2MA_x\text{-}OEGMA_{100-x})$ (where x and 100-x represent the molar fractions of MEO_2MA and OEGMA, respectively) and loaded with the cancer drug doxorubicine (DOX). The synthesis of SPIONs and the grafting of copolymer on their surfaces were performed following the method reported earlier by Alem *et al.*[43]

The thermo-responsive polymer was engineered to display a LCST around 41°C in physiological medium (PM), above the temperature required for living cells in normal conditions. The drug release kinetic was studied for DOX and the release profile was dependent of the temperature and the time in culture medium. The drug release occurred around 42°C with a cumulative DOX release around 100% within 52 h. It has been also shown that such prepared drug-loaded magnetic MNPs displayed magnetic hyperthermia properties as heat was delivered when an alternating magnetic field was applied.

The cytotoxicity results showed that the core/shell MNPs exhibit limited cytotoxicity towards SKOV-3 up to concentration of 12 $\mu g.mL^{-1}$. When loaded with DOX, upon its release, MNPs were much more cytotoxic towards those cells than the free DOX.

2. MATERIALS AND METHODS

2.1 Chemicals

All reagents were purchased from Sigma-Aldrich, excepted ((chloromethyl)phenylethyl)trimethoxysilane (CMPETMS) (Gelest,> 95%). All the reagents were used as received.

The synthesis of sodium citrate stabilized $Fe_{3-\delta}O_4$ MNPs was carried out using iron (III) chloride hexahydrate (Lancaster, 98%), iron (II) sulfate heptahydrate (Merck, 99.5%), ammonia solution (NH_3, 28%-30% w/v) and sodium citrate (99.8%), which were all purchased from Sigma-Aldrich. To graft the polymerization initiator, ((chloromethyl) phenylethyl) trimethoxysilane (CMPETMS) (Gelest,> 95%), tetramethylammonium hydroxide pentahydrate (TMAOH) (VWR chemicals, 99.8 %) and toluene (Laboratory Reagent, > 99.3%) were used. To conduct the grafting of the $P(MEO_2MA_X\text{-}$

$OEGMA_{100-X}$) by surface initiated polymerization, the, 2-(2-methoxy) ethyl methacrylate (MEO_2MA) (98 %), oligo (ethyleneglycol) methacrylate (OEGMA) (98 %), N, N-Dimethylformamide (DMF) (>99.8%), Dimethylsulfoxide (DMSO) (>99.8%) and Milli-Q water, from Sigma-Aldrich were used. The biological studies were performed in Dulbecco's Modified Eagle Medium high glucose (DMEM; Sigma Aldrich, Saint-Louis) for the cells growth, supplemented with 15% Fetal Bovine Serum (FBS; Sigma-Aldrich, Saint-Louis), 100 U/mL penicillin, 100 $g.mL^{-1}$ streptomycin, 4 mM L-glutamine, and 0.25 $\mu g.mL^{-1}$ of amphotericin B. Cell were grown in an incubator at 37°C, 5% CO_2 atmosphere, and humidity.

2.2 Synthesis of $Fe_{3-\delta}O_4$ MNPs

Superparamagnetic $Fe_{3-\delta}O_4$ nanocrystals were synthesized by coprecipitation. A mixture of $FeCl_3.6H_2O$ (6 mmol; 1.622 g) and $FeSO_4.7H_2O$ (5 mmol; 1.39 g) was dissolved in 40 mL water in a three necked round bottom flasks. 5 mL of a 28% (v/v) aqueous ammonia solution were subsequently added to the mixture and the final solution was heated at 90°C under argon atmosphere with magnetic stirring. Then, 4.4 g (14.9 mmol) of sodium citrate in 15 mL water were added dropwise until getting a black solution. The reaction mixture was further stirred for 30 min. $Fe_{3-\delta}O_4$ SPIONs were finally recovered by magnetic separation, washed several times with ethanol and redispersed in 100 mL water.

2.3 Synthesis of CMPETMS-coated $Fe_{3-\delta}$ O_4 MNPs ($Fe_{3-\delta}$ O_4@silane)

SPIONs were dispersed in 10 mL of toluene under argon. CMPETMS (0.2 mmol, 49.1 µL) was injected and the mixture stirred for 2 min. Then, 1 mL of an ethanolic solution of tetramethylammonium hydroxide pentahydrate (TMAOH) (36.25 mg) was added and the mixture further stirred under argon for 15 min at 50°C. The mixture was then cooled to room temperature and SPIONs were separated by centrifugation and washed two times with toluene. The silanized SPIONs were dispersed in 10 mL of toluene and 2 mL of an ethanolic solution of TMAOH (36.25 mg) were injected.

The reaction was conducted under argon for 30 min at 50°C under magnetic stirring. The mixture was cooled in a water bath and SPIONs were separated by centrifugation and washed two times with toluene.

2.4 Synthesis of $Fe_{3-\delta}O_4$@P(MEO_2MA_X-$OEGMA_{100-X}$)

The growth of P(MEO_2MA_X-$OEGMA_{100-X}$) from iron oxide MNPs surface was conducted using an adapted protocol described by Alem *et al.*[43] Briefly, in a 100 mL Schlenk flask, 50 mg of $Fe_{3-\delta}O_4$@silane MNPs were dispersed in 10 mL of a DMF/DMSO mixture (10/90, v/v). 1.6 mL of MEO_2MA and 1.14 mL of OEGMA were added for the synthesis of $Fe_{3-\delta}O_4$@P(MEO_2MA_{60}-

$OEGMA_{40}$) 1.26 mL of MEO_2MA, 1 mL of OEGMA for $Fe_{3-\delta}O_4$@P(MEO_2MA_{65}-$OEGMA_{35}$). Once the MNPs were completely dispersed, 200 mL of $CuBr_2$/TPMA (0.884 mmol $CuBr_2$, 4.3 mmol TPMA) stock solution in DMSO were added to the mixture. The reaction mixture was stirred and heated to 65 °C. Next, 250 mL of a stock solution of hydrazine in DMSO (7.1 $mg.mL^{-1}$) were added and the mixture was stirred for 2 h at 65 °C with argon. At the end of the polymerization, the mixture was poured drop by drop into hot Milli-Q water to precipitate the insoluble components. The materials were purified by redispersion of the core/shell MNPs in cold water followed by centrifugation of the solution after heating.

2.5 Drug conjugation to MNCs

Conjugation of DOX with the MNPs was achieved through formation of hydrogen bonds with the ether-oxyde groups of P(MEO_2MA-OEGMA) copolymer (as illustrated in Figure 6). DOX and MNCs were mixed in DMEM (pH = 7.4) and the mixture was gently shaken in the dark for 24 h at room temperature, thereby leading to the conjugation of DOX via imine linkage. The DOX-loaded MNCs (DOX-MNCs) were retrieved by magnetic separation and washed thoroughly with DMEM until no DOX was detected in the supernatant (at least 10 washing cycles). The concentration of released DOX as a function of time (at 37 and 42°C) was calculated by measuring the absorbance of the supernatant at 480 nm of the free DOX remaining in solution. The drug loading content (DLC), drug loading efficiency (DLE), and percentage of drug released (%) could then be calculated from Eqs. (1), (2) and (3),

$$\text{DLC (wt \%)} = \frac{\text{amount of DOX in the MNPs}}{\text{amount of MNPs}} \times 100 \quad (1)$$

$$\text{DLE (wt \%)} = \frac{\text{amount of DOX in the MNPs}}{\text{total amount of feeding drug}} \times 100\% \quad (2)$$

$$\text{percentage of drug released} = \frac{\text{mass of drug released}}{\text{mass of drug loaded}} \times 100\% \quad (3)$$

2.6 Characterization methods

Dynamic light scattering (DLS) was performed at room temperature using a Malvern Zetasizer HSa instrument with an He–Ne laser (4×10^{-3} W) at a wavelength of 633 nm. The MNPs aqueous solutions were filtered through Millipore membranes (0.2 mm pore size). The data were analyzed by the CONTIN method to obtain the hydrodynamic diameter and size distribution in each aqueous dispersion of MNPs. For Transmission Electron Microscopy (TEM) experiments, one drop of a dispersed solution of MNPs was deposited on holey carbon grids and imaged. The Microscope used was an ARM 200F. The crystallographic structure of the MNPs was identified by X-Ray Diffraction (XRD) using a Philips PW3710 diffractometer with Cu Kα radiation. Fourier-transform infrared (FTIR) measurements were conducted (i) on powders by using a Nicolet 6700 FTIR spectrometer equipped with a deuterated triglycine sulphate (DTGS) detector in the 400–7000 cm^{-1} wavelength range (i.e., 1.24–25 mm) in a reflexion mode (ii) on suspensions in DMEM with a Bruker Vertex 70v using a nine-reflection diamond ATR accessory (DurasamplIR™, SensIR Technologies, incidence angle: 45°). A SETSYS Supersonic thermobalance (SETARAM) was used for thermogravimetric measurements. The furnace made of graphite element operates from room temperature up to 1600°C. The apparatus was controlled by software appointed Calisto. Dry samples of 30 mg were put in an alumina crucible with a volume of 30 mL. The samples were heated from room temperature to 600°C at an heating rate of 5°C min^{-1} under argon atmosphere. The magnetic properties of the core/shell MNPs were studied by superconducting quantum interference device SQUID-VSM combined to Vibrating Sample Magnetometer.

2.7 In vitro magnetic hyperthermia

Heat capacity measurements:

Heat capacities of mixtures at atmospheric pressure were measured using a Calvet type calorimeter, Setaram C80 (France) in a range of temperature from 298 to 373.15 K. A full description of the procedure is given in previous work.[44,45] In few words, the sample temperature was first fixed at 298 K during 2h. Then, a scanning rate was set to 0.5 K min^{-1} up to 373 K. This temperature was maintained during 1h.

Magnetic hyperthermia measurements:

Magnetic heating measurements were performed to assess the heating performances of the nanocomposites using a magnetic hyperthermia induction apparatus composed of a DM 100 instrument and DM applicator (Nanoscale BiomagneticsTM, nB), under MaNIaC software. The system was set to operate at a frequency f = 536.5 kHz and field amplitude H = 300 Gauss. Samples made of 1 mL of $Fe_{3-\delta}O_4$@P(MEO_2MA_X-$OEGMA_{100-X}$) dispersed in water (DMEM) with a concentration of 4.5 mg mL^{-1} were placed in the middle of the coil. The increase in temperature was continuously logged using

optic fiber probes centered in the suspension. The measurement started when the temperature of the suspension was stabilized at room temperature, and the measurement time was limited to 10 min. The specific absorption rate (SAR) was commonly employed to quantify the heat dissipation rate of a given ferrofluid, even though it was not an intrinsic property of the system as it was strongly dependent upon the frequency and field amplitude used during the measurement. First, a second order polynomial function was used to fit the plot over the first 120 seconds and determine [dT/dt]t=0. In the fitted plot $\Delta T\ (t) = intercept + a \times T + b\ \times T^2$, the a value corresponds to [dT/dt]t=0 as detailed by Perigo et al[7]. This allows to finally calculate the SAR value by using the following equation:

$$\mathrm{SAR} = \frac{\mathrm{C}}{\mathrm{m_{Fe}}}\frac{\Delta \mathrm{T}}{\Delta \mathrm{t}} \tag{4}$$

where C denotes the specific heat capacity of the sample, m_{Fe} is the iron mass per unit volume of liquid and ΔT/Δt represents the initial temperature rise rate. The SAR was then calculated in regards to iron oxide mass.

2.8 DOX release kinetics studies

In order to determine the mechanism of drug release and the release rate, the data obtained were fitted with the most relevant kinetic models for our system, such as zero-order, first-order, Higuchi and Korsmeyer−Peppas release models[16].

The zero-order kinetic release is concentration dependent and can be expressed as:

$$\boldsymbol{M_t = M_0 + K_0 . t} \tag{5}$$

where M_t is the amount of drug dissolved in time t, M_0 is the initial amount of drug in the solution (M_0 = 0) and K_0 is the zero order release constant expressed in units of concentration/time.

The first order kinetic release is concentration dependent and can be expressed as

$$\boldsymbol{M_t = M_\infty[1 - exp(-K_1 . t)]} \tag{6}$$

where M_0 is the initial concentration of drug, K_1 is the first order rate constant, and t is the time.

Higuchi model describes a drug release from solid matrices as:

$$M_t = K_h \cdot t^{1/2} \quad (7)$$

where M_t is the drug released at time t, and K_h is the rate constant. Once a plot of $M_t/t^{1/2}$ is linear with a slope ≥1, it is considered to follow the Higuchi drug release kinetics.

Korsmeyer–Peppas model consists in a simple relationship, which describes a drug release from a polymeric matrix, and written as:

$$\frac{M_t}{M_\infty} = K_{kp} \cdot t^n \ , \ \frac{M_t}{M_\infty} < 0{,}6 \quad (8)$$

where M_t/M_∞ is the drug release fraction at time t; K_{kp} is a constant; and n is the release exponent. The release model follows Fickian diffusion as $n \leq 0.5$, while non-Fickian as $0.5 < n < 1$[16]. By comparing the regression coefficient (R^2) of the different model, the accuracy of each fitting could be verified. For each temperature, the model giving the highest R^2 was considered as the best fit of the release data.

2.9 Biological Characterization

The human ovarian adenocarcinoma cell line SKOV-3 was obtained from ATCC® (LGC Promochem, Molsheim, France). Cells were grown in humidified atmosphere, 5 % CO_2, at 37°C in Dulbecco's Modified Eagle's Medium (DMEM) without phenol red (Invitrogen, Cergy-Pontoise, France), supplemented with 9 % heat-inactivated fetal calf serum (FCS) and 1 % 200 mM L-glutamine (Life Technologies, Carlsbad, USA). Three days before adding the MNPs, SKOV-3 cells were trypsinized, recovered in supplemented DMEM and seeded in 96-well plate at 10^5 cells.mL^{-1} ($2.5*10^4$ cells per well). Cells were exposed to free DOX (range 1.3-10 µg.mL^{-1}), $Fe_{3-\delta}O_4$@P(MEO_2MA_{60}-$OEGMA_{40}$) (range 0.78-12.5 µg.mL^{-1}) or DOX-loaded $Fe_{3-\delta}O_4$@P(MEO_2MA_{60}-$OEGMA_{40}$) (range 1.3-10 µg.mL^{-1} MNPs) for 24h at 37°C or 5h at 41 °C.

Cell viability was assessed by the MTT [3-(4,5-dimethylthiazol-2-yl)-2,5-diphenyl-2H-tetrazolium bromide; Sigma] colorometric assay, which measures the capacity of mitochondrial deshydrogenase in viable cells to reduce MTT to purple formazan crystals. Following incubation, cells were washed twice with cold PBS, fresh medium was added, and cells were maintained in an incubator. 24 h later, the medium was removed, the MTT solution was added to each well, and cells were placed in an incubator for 3h. The formazan crystals were solubilized by adding dimethyl sulfoxide and absorbance was measured at 540 nm with a plate reader (Ascent Multiskan). Cell death percentage was obtained by referring the treated samples to control non-treated cells.

3. RESULTS AND DISCUSSION

3.1 Characterization of P(MEO_2MA_x-OEGMAy) growth from SPIONS

The efficiency of the growth of P(MEO_2MA_X-$OEGMA_{100-X}$) by ARGET-ATRP process from $Fe_{3-\delta}O_4$@Silane surface as illustrated in Figure 1, was confirmed by FTIR. The spectrum of MNPs shows two broad bands at 1556 and 1394 cm^{-1} mainly assigned to the carboxylate group from the remaining citrates groups. The band at 1247 cm^{-1} was assigned to the Si-CH_2-R groups near the core and the overlapped bands between 1150 and 1000 cm^{-1} were assigned to the stretching bands from C-OH, Si-O-Si and Si-O groups. Concerning the polymer chain chemical signature, absorption bands located at 1720 and 1110 cm^{-1} are assigned to the ester C=0 and C-O bonds stretching of the repeatitive unit moities of the P(MEO_2MA_x-$OEGMA_{100-x}$) (see Figure SI 1).

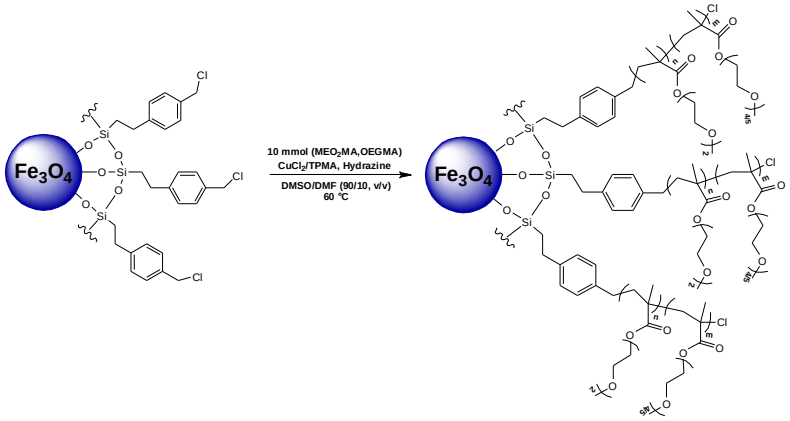


Figure 1: Schematic illustration of the synthetic process for the preparation of $Fe_{3-\delta}O_4$@P(MEO_2MA_X-$OEGMA_{100-X}$) MNPs.

The amount of copolymer anchored at the MNPs surface is of importance as it is directly linked to the amount of drug that can be loaded within the core/shell MNPs. Thermogravimetric analysis were conducted, and as can be seen in Figure 2, depending on the ratio MEO_2MA/OEGMA, the amount of the grafted polymer varied from 38% for the $Fe_{3-\delta}O_4$@P(MEO_2MA_{65}-$OEGMA_{35}$) to 43% for the $Fe_{3-\delta}O_4$@P(MEO_2MA_{60}-$OEGMA_{40}$), the reference being the $Fe_{3-\delta}O_4$@Silane MNPs. This high calculated amount of copolymer confirms the advantage of the use of grafting-from process (growth of the macromolecule from the MNPs surfaces) compared to the grafting-to process (grafting of the co-polymer after its synthesis) that has been shown to lead to amounts of polymer varying between 8 to 15% at the surface of the MNPs.[15,30]

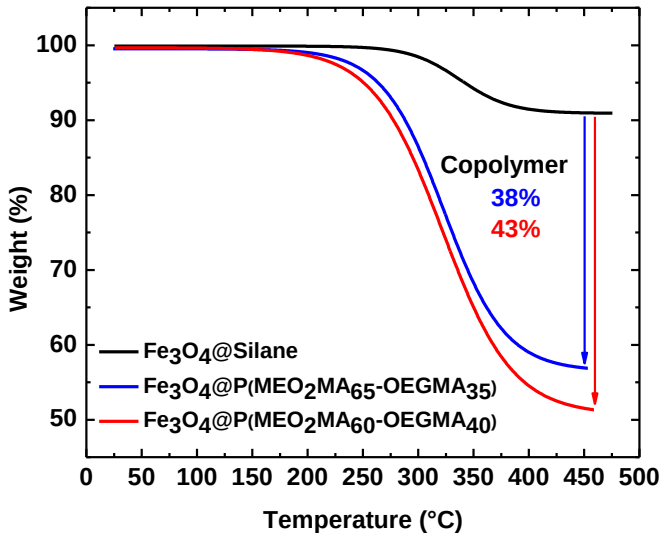


Figure 2. TGA-DTA analysis in N_2 atmosphere.

3.2 Core/shell MNPs microstructure

To study the microstructure of the MNPs, TEM and High Resolution-Transmission Electron Microscopy (HR-TEM) experiments were performed. In figure 3a the TEM micrographs of $Fe_{3-\delta}O_4$@P(MEO_2MA_{60}-$OEGMA_{40}$) confirmed the spherical shape of MNPs with an average size of 10 ± 1.5 nm (calculated from TEM images). Moreover, the well coverage of the MNPs surfaces by the copolymer could be studied by HR-TEM combined with Energy Filtered-Transmission Electron Microscopy (EF-TEM) analysis. The elemental signal of carbon (in white, Figure 3d) was detected at the surface and at the interspace between particles indicating the presence of the co-polymer around the magnetic MNPs.

Sharp and clearly defined peaks can be observed on the XRD pattern (Figure SI2 in the Supporting Information), which indicates a high degree of crystallinity for the MNPs. The diffraction peaks match with the formation of a spinel iron oxide phase. The calculated lattice parameter is 0.841 nm by comparison with those of Fe_3O_4 magnetite phase of 0.8396 Å (JCPDS PDF no. 00-019-0629) and the maghemite one γ-Fe_2O_3 (0.8346 Å, JCPDS file 39-1346). A mean crystallite size of 11.3 nm was calculated from the XRD pattern by the application of the Scherrer equation to the broadening of the (311) reflection signal, which is in good agreement with the particle size determined from TEM micrographies (Figure 3a).

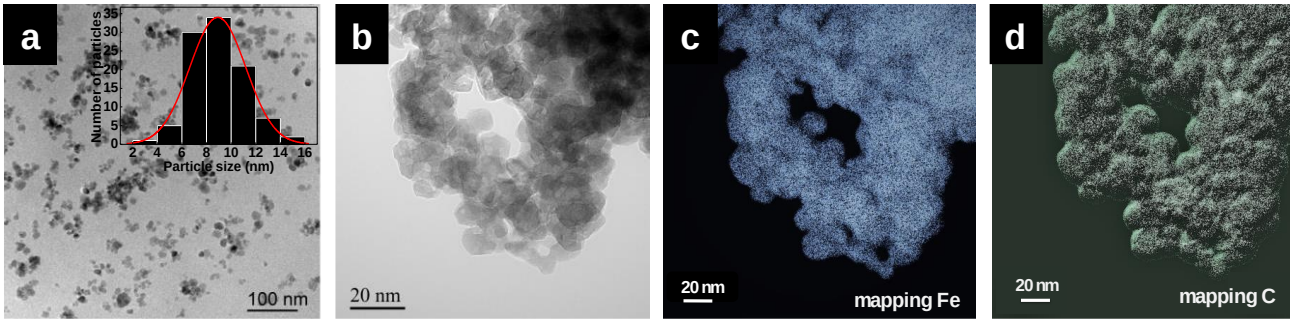


Figure 3. (a) TEM micrographs of $Fe_{3-\delta}O_4$@P (MEO_2MA_{60}-$OEGMA_{40}$) MNPs. (b) Fe mapping images of $Fe_{3-\delta}O_4$@P (MEO_2MA_{60}-$OEGMA_{40}$) MNPs obtained by EF-TEM, (c) C mapping images of $Fe_{3-\delta}O_4$@P (MEO_2MA_{60}-$OEGMA_{40}$) MNPs obtained by EF-TEM.

Superparamagnetic properties of the core/shell MNPs

The superparamagnetic properties of the SPIONs at room temperature and as a function of temperature could be verified by the zero field cooled-field cooled (ZFC-FC) measurements. As depicted in Figure 4a, the maximum of ZFC curve assimilated to the blocking temperature is at around 250 K, which is largely below the physiological temperature range. This blocking temperature is slightly larger than that was reported for other iron oxide nanoparticles with similar sizes which suggested some aggregation of nanoparticles. Indeed the presence of dipolar interaction induced a shift of the blocking temperature towards higher temperature[46,47]. The saturated magnetization of the $Fe_{3-\delta}O_4$@P(MEO_2MA_{60}-$OEGMA_{40}$) and $Fe_{3-\delta}O_4$@P(MEO_2MA_{65}-$OEGMA_{35}$) MNPs are 30 $emu.g^{-1}$ and 33 $emu.g^{-1}$, respectively, and are lower values than the one for the uncoated $Fe_{3-\delta}O_4$ MNPs (80 $emu.g^{-1}$) (Figure SI3 in the Supporting Information). This can be attributed to a decrease in the magnetic interaction with diamagnetic coating. Despite of a decrease of the magnetization, all the MNPs quickly and firmly interact with a magnet (inset in Figure 4b).

Moreover, this superparamagnetic behavior was evaluated at 5 K and 300 K. At 5 K, an hysteresis cycle can be observed due to the transition to a low temperature blocked state with a saturation magnetization of 80 $emu.g^{-1}$ and a coercive field of about ≈ 270 Oe. Oppositely, at 300 K, no coercive field is observed and a saturation magnetization of 70 $emu.g^{-1}$ is obtained for the nude $Fe_{3-\delta}O_4$ MNPs (Figure SI3 in the Supporting Information)

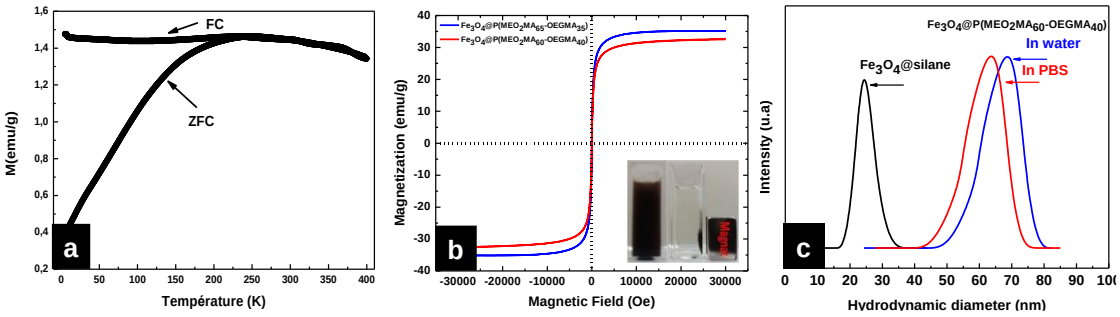


Figure 4. Characterization of NPs, hydrodynamic diameter, and magnetization properties. (a) Hydrodynamic diameter distribution of bare and $Fe_{3-\delta}O_4$@P (MEO_2MA_{60}-$OEGMA_{40}$) MNPs in water and PBS and (b) Magnetization curve of (MEO_2MA-$OEGMA_{100-X}$)-capped $Fe_{3-\delta}O_4$ NPs at 300 K (c) ZFC/ FC curves of $Fe_{3-\delta}O_4$@P(MEO_2MA_{60}-$OEGMA_{40}$), B = 75 Oe.

Colloidal behavior of the core/shell nanoparticles (in water and in vitro)

In order to translate those MNPs into clinical applications, a major point is their stability in physiological media. Indeed, contrary to pure water, these media are composed of different salts and proteins that can influence the colloidal behavior of the MNPs. Firstly, the $Fe_{3-\delta}O_4$@Silane (in ethanol) displayed an hydrodynamic diameter of about 20-30 nm. In water, the measured P(MEO_2MA_X-$OEGMA_{100-X}$) hydrated coating (~ 55-80 nm in water and ~ 50-75 nm in PBS) which confirms a moderate aggregation (Figure 4a). It is worth to mention that MNPs with sizes varying between 10 and 200 nm preferentially accumulate into tumor than in healthy tissue due to the enhanced permeability and retention effect (EPR).[13,17] Owing to the porous vascular architecture of the tumors and the degradation of the lymphatic clearance, the MNPs diffusion in tumor tissue would be largely enhanced. The 50–80 nm hydrodynamic diameters of the MNPs developed in this work seem then optimal for EPR effect.

The responsive behavior and the starting temperature at which the MNPs started to aggregate were also monitored by DLS. As depicted in Figure 5, when a solution of $Fe_{3-\delta}O_4$@P(MEO_2MA_{60}-$OEGMA_{40}$) and $Fe_{3-\delta}O_4$@P(MEO_2MA_{65}-$OEGMA_{35}$) MNPs is heated from 25 to 50°C, their hydrodynamic diameter started to increase at 38 and 41°C, respectively, which corresponds to the LCST's of P(MEO_2MA_{60}-$OEGMA_{40}$) and P(MEO_2MA_{65}-$OEGMA_{35}$) in physiological medium (DMEM), respectively. To confirm the complete reversibility of the processes, five successive cycles of heating (T > LCST) and cooling (T < LCST) were conducted (Figure SI 4). A reversible behavior in physiological medium upon heating and cooling was demonstrated for the entire sample. This behavior

is in perfect agreement with the high hydration capacity of the ethylene glycol groups below the collapse temperature and the chains shrinking above the latter.[18,19]

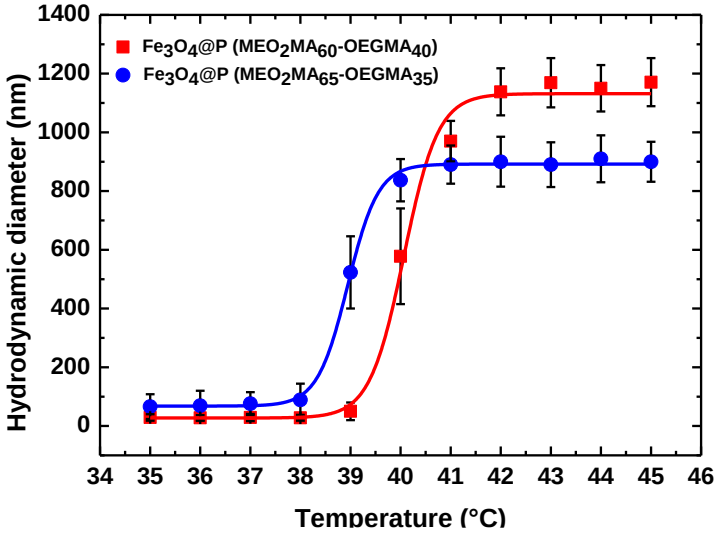


Figure 5: DLS data of $Fe_{3-\delta}O_4$@P (MEO_2MA_{60}-$OEGMA_{40}$) (red) and $Fe_{3-\delta}O_4$@P (MEO_2MA_{65}-$OEGMA_{35}$) (blue) MNPs in DMEM from 35 to 45°C.

3.4 DOX loaded nanoparticulate systems studies

3.4.a. Interaction between the DOX and the NPs responsive shell

To enlighten the interaction between the doxorubicine and the copolymer chains, FT-IR experiments were conducted, and Figure 6 shows the FTIR-ATR spectra of DOX, MNPs and NPs-DOX recorded in DMEM medium The assignments were performed according to the literature[49–51]. The spectrum of DOX (Figure 6 a) shows well-defined bands at 1582, 1285, 1269, 1211, 1013 and 990 cm^{-1} assigned to the aromatic moieties of DOX. In addition, the bands at 1724 and 1624 cm^{-1} were assigned to the C=O stretching band and NH_2 bending band, respectively.Which clearly differe from the core/shell MNPs as described above. The spectrum of MNPs after contact with DOX and subsequent rinsing shows bands at 1285, 1266, 1211, 1015 and 995 cm^{-1}. They are assigned to the aromatic moieties of DOX, and they ascertain the occurrence of DOX on MNPs. The C=O stretching band absorbs at 1741 cm^{-1} in DOX-MNPs showing probably different hydrogen bonding of the DOX ester group. One interesting feature of the spectrum is the disappearance of the NH_2 bending band previously observed at 1624 cm^{-1}. It strongly suggested that this band was displaced in the region between 1550 and 1580 cm^{-1} were several overlapping bands are observed. This shift is due to strong hydrogen bonding involving the amine group from DOX and the ether oxydes polar groups of the copolymer.

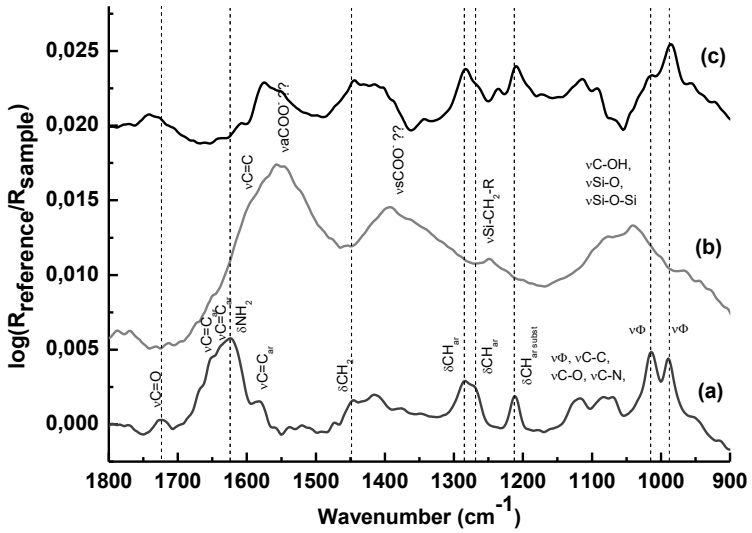


Figure 6: FTIR spectra in ATR mode of (a) DOX, (b) MNPs, and (c) MNPs-DOX in DMEM medium (reference = DMEM medium in which the species are)."

3.4b DOX release profile and mechanism as a function of temperature

DOX was chosen as a drug model to determine the drug-release properties of MNPs. The copolymer responsive behavior translates in the fact that upon reaching the LCST, the polymer becomes hydrophobic and shrinks by expelling solvating water molecules. We have shown that DOX interact with the co-polymer polar ether-oxydes moieties via hydrogen bonding, as the water molecules. We assumed that DOX molecules are pushing out the water molecules whereas interacting with the polymer backbone. The drug carrier at different temperatures showed sustained drug release properties in biological media with different release rates. As expected, the release process at 37°C was much slower than at 42°C. In culture medium, after incubation at 37°C, the initial proportion of DOX cumulative release from $Fe_{3-\delta}O_4$@P(MEO_2MA_{60}-$OEGMA_{40}$) MNPs was 0% within almost 10 hours (figure 7a). The amount of released DOX increased slowly with time and a change in the slope appeared after 25 h of incubation in culture medium. This change can be related to the presence of different entities in the culture medium such as proteins and salts, that may act as kosmotropic species (lead to an early expelling of water molecule from the grafted polymer chains which results in a premature collapsing of the polymer-chain[24]), and thus inducing the early DOX-polymer bond breaking with time. Finally, after 54 h, the released DOX is 80%.

At 42°C, a linear increase of drug release with time was observed. As for the studies at 37°C, the drug release profile with time was not an on/off system. An initial burst release of 20% was observed for

the DOX-$Fe_{3-\delta}O_4$@P(MEO_2MA_{60}-$OEGMA_{40}$) MNPs followed by a linear increase with time until reaching 100% after 54 h.

Nevertheless, the influence of temperature on the drug delivery process can be clearly seen as the DOX release rate and amount are much higher at 42°C than 37°C with time (Figure 7). The same trend of the cumulative DOX release with time was observed for DOX-$Fe_{3-\delta}O_4$@P(MEO_2MA_{65}-$OEGMA_{35}$) MNPs. The $Fe_{3-\delta}O_4$@P(MEO_2MA_{65}-$OEGMA_{35}$) MNPs display a LCST at 38°C in physiological medium, at 37°C the maximum of DOX release (70%) is reached (after 30 h) and an initial burst of 40% is observed at 42°C.

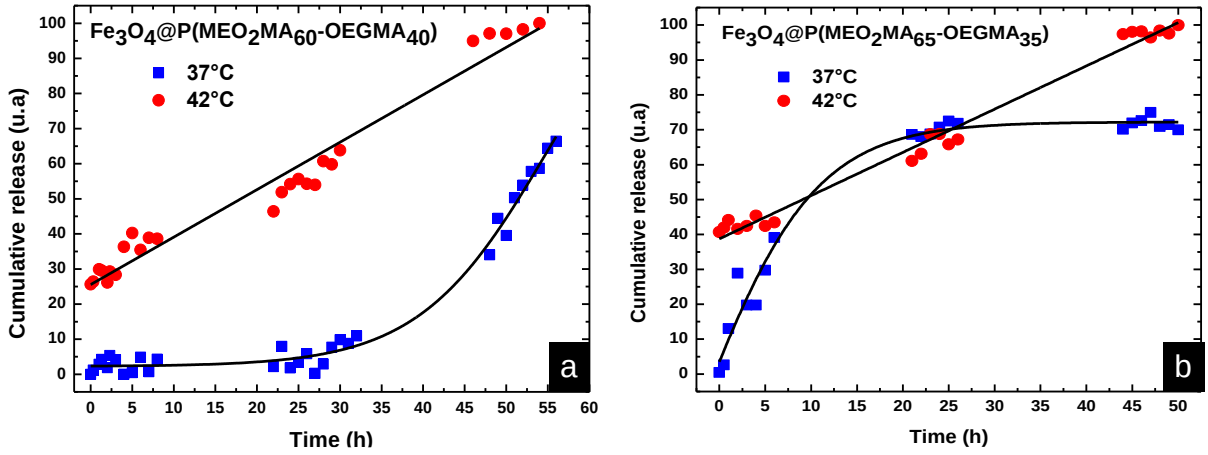


Figure 7. Release of DOX from $Fe_{3-\delta}O_4$@P (MEO_2MA_{60}-$OEGMA_{40}$) and $Fe_{3-\delta}O_4$@P (MEO_2MA_{65}-$OEGMA_{35}$) MNPs in physiological medium (DMEM).

The release kinetics and mechanism of DOX from the magnetic MNPs were determined according to the mathematical models previously described. The release parameters for each model (K_1, K_h, K_{kp} and n) are shown in Table 1 as well as the correlations values (R^2), which enabled the extraction of an equation for each system in function of temperature (eq. 9-12). The MNPs display two different release behaviors depending on the temperature. At 37°C, the Zero order kinetics, Higuchi kinetics and Korsmeyer–Peppas model do not fit well with experimental data as manifested by low R^2 values, whereas the first order kinetics seems to be the best illustrating model for our systems at 37°C (see eq. 9 and 10) . Furthermore, the linear increase in drug release at 42°C shows that the Zero Order kinetics is the most relevant model to illustrate the DOX release behavior from the core/shell MNPs above the copolymer LCST (see eq. 11 and 12).

Table 1. Kinetics data of DOX release from the core-shell MNPs.

		Zero Order		First Order		Higushi		Korsmeyer-Peppas		
Samples	T°(C)	K_1	R^2	K_1	R^2	K_h	R^2	K_{kp}	n	R^2
$Fe_{3-\delta}O_4$@ P(MEO_2MA_{65}-$OEGMA_{35}$)	37°C	0.0019	0,7180	1.4254	0.9603	1.1012	0.8461	0.5765	0.3825	0.8468
$Fe_{3-\delta}O_4$@ P(MEO_2MA_{60}-$OEGMA_{40}$)	37°C	0.003	0,830	0.003	0.988	0.826	0.668	0.911	0.277	0.823
$Fe_{3-\delta}O_4$ @P(MEO_2MA_{65}-$OEGMA_{35}$)	42°C	1.2382	0,9874	1.7473	0.9842	0.4449	0.8060	0.6466	0.2224	0.8060
$Fe_{3-\delta}O_4$ @P(MEO_2MA_{60}-$OEGMA_{40}$)	42°C	4.137	0,989	0.018	0.988	0.090	0.859	0.556	0.290	0.860

The associated equations for each system are the following:

For $Fe_{3-\delta}O_4$@P(MEO_2MA_{60}-$OEGMA_{40}$)-DOX à 42°C :

$$\boldsymbol{C_{60/40}^{42°C}}(\%) = 1{,}3516t + 25.5716 \quad (9)$$

For $Fe_{3-\delta}O_4$@P(MEO_2MA_{65}-$OEGMA_{35}$)-DOX à 42°C :

$$\boldsymbol{C_{65/35}^{42°C}}(\%) = 1.2382\text{t} + 38.7545 \quad (10)$$

For $Fe_{3-\delta}O_4$@P(MEO_2MA_{60}-$OEGMA_{40}$)-DOX à 37°C

$$C_{60/40}^{37°C}(\%) = 0{,}0075.\exp(\frac{t}{16.5}) + 0{,}01324 \quad (11)$$

For $Fe_{3-\delta}O_4$@P(MEO_2MA_{65}-$OEGMA_{35}$)-DOX à 37°C

$$C_{65/35}^{37°C}(\%) = -0{,}1181.\exp(-\frac{t}{8{,}5}) + 0{,}1659 \quad (12)$$

Where $C_{y/z}^{x°C}(\%)$ represents the percentage of cumulative of DOX release, x the degree at which the release experiment were performed, and y the amount of MEO_2MA and z the amount of OEGMA.

Moreover, Drug Loading Capacity (DLC, wt%) and the Drug Loading Efficiency (DLE, wt%) of the core/shell MNPs could reach 6.2% and 56,1 %, respectively, for $Fe_{3-\delta}O_4$@P($MEO2MA_{60}$-$OEGMA_{40}$). Close results were also obtained for $Fe_{3-\delta}O_4$@P(MEO_2MA_{65}-$OEGMA_{35}$) (DLC of 5.7% and DLE of 57%). All results were extracted from UV curves and data shown in Supp Info Figure SI 5. The DLC values were close to those we can find in the literature[52], but the DLE values were lower compared to literature data[52]. This can be attributed to the encumbered branched structure of OEGMA that impairs the diffusion of DOX compared to other polymers like PEG whose linear structure allows an easier diffusion of DOX.

3.4 c. DOX loaded-nanoparticulate system stability at 20°C study

DOX (1mg.mL^{-1}) and MNPs (0.03 mg.mL^{-1}) were incubated in DMEM at 20°C, once the excess of DOX removed , the resulting hydrodynamic diameter of the DOX-loaded system was measured by DLS for 72 h. All results are gathered in Figure SI 7, which shows that considering the error bars, the diameters of the DOX-loaded nanoparticles systems do not change within 72 h.

3.5 Magnetic hyperthermia Study

The temperature profiles with time and SAR values measurements obtained at the AC field parameters of H=300 Gauss (23.8 kA.m-1) and f=536.5 kHz of $Fe_{3-\delta}O_4$@P(MEO_2MA_{60}-$OEGMA_{40}$) and $Fe_{3-\delta}O_4$@P(MEO_2MA_{65}-$OEGMA_{35}$) MNPs in water and physiological medium (DMEM) are shown in Figure 8. Magnetic measurements have already shown the superparamagnetic properties of $Fe_{3-\delta}O_4$@P(MEO_2MA_X-$OEGMA_{100-X}$) MNPs (Figure 4). Thus, the primary factor for heat generated by superparamagnetic MNPs is attributed to Brownian and/or Neel's spin relaxations.

Temperature profile curves show a gradual increase in temperature for the samples in water and physiological media (Figure 8). The required magnetic hyperthermia temperature (i.e., 41-45°C) can be then achieved as an increase of temperature can be reached within less than 7 minutes for the $Fe_{3-\delta}O_4$@P(MEO_2MA_X-$OEGMA_{100-X}$) MNPs in physiological media at low applied AC magnetic field (23.8 kA/m, and f = 536.5 KHz). The $Fe_{3-\delta}O_4$@P(MEO_2MA_X-$OEGMA_{100-X}$) MNPs disperse more easily in physiological media than in water. From Figure 8, it could be observed that the SAR increased with the polymer density and depends on the solvent. The obtained SAR in physiological media for the $Fe_{3-\delta}O_4$@P(MEO_2MA_{65}-$OEGMA_{35}$) and $Fe_{3-\delta}O_4$@P(MEO_2MA_{60}-$OEGMA_{40}$) MNPs were ~45.7 $W.g^{-1}$ and ~12.6 $W.g^{-1}$ compared to ~61.7 $W.g^{-1}$ and ~25.2 $W.g^{-1}$ in water (Table 2), respectively. Compared to the bare $Fe_{3-\delta}O_4$ MNPs (MNPs before silanisation), the SAR which is of ~100 $W.g^{-1}$ and ~101 $W.g^{-1}$ in water and culture media, respectively, is decreased despite the remaining good dispersion in water after the copolymer functionalization.

As shown in Figure 5, until 36°C there is no aggregation of the MNPs in water (or in culture media), but it has to be considered that during the measurements, we collected the temperature of the whole solution (MNPs with aqueous media), whereas a local heating of the MNPs has to be considered[7]. This local heating may reach 50°C, which should induce the collapse of the polymer chain (see Figure 5) and then the further aggregation of the MNPs. This MNP aggregation by limiting heat transfer finally explains the decrease of at least by two the SAR as observed in other studies[7].

Concerning the influence of the medium, it is clear that when the core/shell MNPs are dispersed in the culture medium, the SAR decreased. We have shown that the colloidal behavior of the core/shell MNPs is driven by the copolymer chains grafted at their surfaces. When dispersed in cultured medium (DMEM), the salts within the culture medium disrupt the hydration structure that surround the polymer chains and thus decrease the hydrophilicity of the final core/shell structure.[20] The direct consequence is that the final dispersion of the MNPs will be less efficient and SAR will decrease.

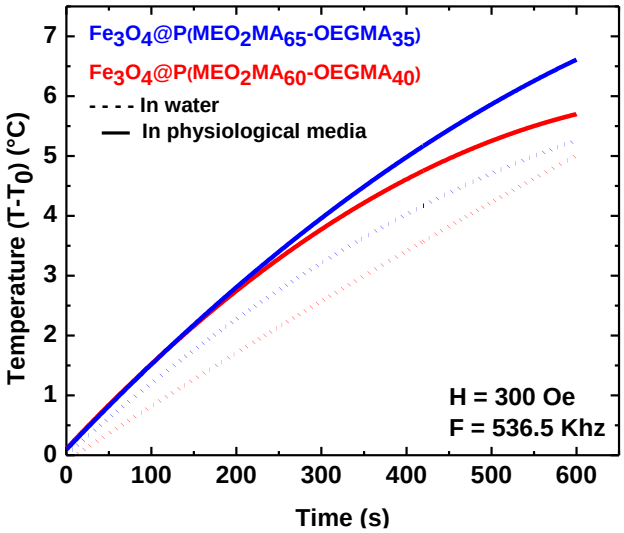


Figure 8. Temperature of $Fe_{3-\delta}O_4$@P (MEO_2MA_X-$OEGMA_{100-X}$) MNPs under AC magnetic field

Samples	**SAR (W/g) in water**	**SAR (W/g) in physiological media**
$Fe_{3-\delta}O_4$@P (MEO_2MA_{65}-$OEGMA_{35}$)	61.7	45.7
$Fe_{3-\delta}O_4$@P (MEO_2MA_{60}-$OEGMA_{40}$)	25.2	12.6

Table 2 : SAR values in water and physiological medium for $Fe_{3-\delta}O_4$@P(MEO_2MA_{65}-$OEGMA_{35}$) and $Fe_{3-\delta}O_4$@P(MEO_2MA_{60}-$OEGMA_{40}$)

3.6 Cytotoxicity Study

Cytotoxicity towards human colon adenocarcinoma cell line HT29

The cytotoxicity of $Fe_{3-\delta}O_4$@P(MEO_2MA_{60}-$OEGMA_{40}$) MNPs was evaluated by conventional MTT assays after incubation with HT29 cells for 24 and 72 h. Figure 9 displays the cell viability after 24 and 72 h exposure to MNPs. The results show that the magnetic core/shell MNPs exhibit a dose-dependent cytotoxicity. Above 12.5µg.mL^{-1}, $Fe_{3-\delta}O_4$@P(MEO_2MA_{60}-$OEGMA_{40}$) MNPs induce a major decrease in cell viability with 85 ± 8% and 75 ± 55 % after 24 h and 72 h, respectively. Chen et al. have proposed a dose-dependent cytotoxicity mechanism for MNPs which involves an increase of the metal ions released when the amount of MNPs increases.[21] Their study highlighted that the leaching of free metal ions from the core/shell MNPs could lead to a high toxicity to cells. However, due to the low solubility of Fe^{2+} ions at physiological pH, the most relevant mechanism that can be considered when $Fe_{3-\delta}O_4$ MNPs get in contact with a tissue, is a mitochondrial disturbance which is translated by an increase of

swelling and cell permeability, and the generation of reactive oxygen species (ROS) with oxidative stress through the Fenton reaction. Our cytotoxicity tests showed that for almost all core/ shell MNPs concentrations, the cytotoxicity decreased with the amount of copolymer grafted at the surface of the MNPs. Therefore, the grafting of co-polymer shell prevents oxidative reactions. However, these MNPs still exhibit a favorable biocompatibility which makes them useful for biomedical applications.

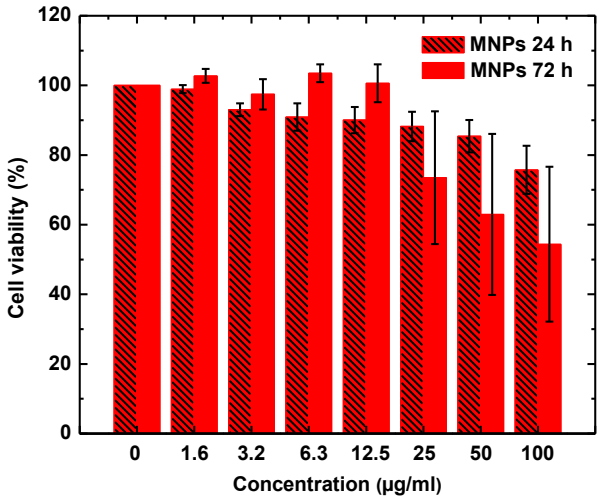


Figure 9. Viability of HT29 cells after (a) 24 and (b) 72 h exposure to $Fe_{3-\delta}O_4$@P (MEO_2MA_{60}-$OEGMA_{40}$) MNPs

3.7 Cell viability after adding non-loaded $Fe_{3-\delta}O_4$@copolymer

Cytotoxicity towards ovarian cancer line SKOV-3

SKOV-3 cell viability after 24 h exposure to $Fe_{3-\delta}O_4$@copolymer MNPs at 37°C or 41°C revealed mild cytotoxicity irrespective of temperature of non-loaded MNPs. Cell viability at 37°C was above 80% even for the highest MNPs dose that produced only an average of ~10% cell death (90.85 ± 10.6% cell viability). At 41°C, the cell viability decreased but remained between 70 and 80 % excepted for the highest MNPs concentration for which 65.08 ± 2.23 % cell viability was observed (Figure 10).

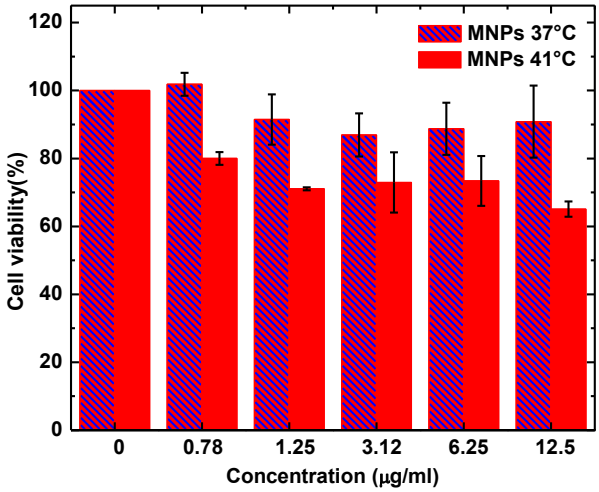


Figure 10. Viability of SKOV-3 in function of the concentration of $Fe_{3-\delta}O_4$@P (MEO_2MA_{60}-$OEGMA_{40}$) MNPs at 37°C and 42°C.

3.8 Cytotoxicity of DOX loaded in $Fe_{3-\delta}O_4$@copolymer compared to free DOX

To study the efficiency of SPIONs responsive MNPs as drug carrier, SKOV-3 cells viability towards DOX was evaluated in different conditions. The $Fe_{3-\delta}O_4$@P(MEO_2MA_{60}-$OEGMA_{40}$) MNPs were selected as drug carrier as they display a LCST in physiological medium above 41°C, whereas the LCST of $Fe_{3-\delta}O_4$@P(MEO_2MA_{65}-$OEGMA_{35}$) NPS is around 38°C, which is too close to the body temperature. In all experiments, we compared the SKOV-3 cells viability when cells were submitted to free DOX (at 0.78 $\mu g.mL^{-1}$) (the results impact of the increased concentration of the DOX on cells depending on the temperature are gathered in figure SI 09) or to DOX incorporated within $Fe_{3-\delta}O_4$@P(MEO_2MA_{60}-$OEGMA_{40}$) MNPs, named MNPs-DOX in the graph Figure 11. All experiments were performed in SKOV-3 cell culture medium at 37°C for 24 h and at 41°C for 5 h (to limit the impact of temperature on cells). Figure 11 shows the percentages of cell viability obtained when cells were exposed to either free DOX or DOX-MNPs for 24 h at 37°C.

The concentration of the DOX release from the NPs is actually very lower that the chosen concentration of the free DOX, but 0.78 $\mu g.mL^{-1}$ was the lower concentration to see an impact of the free DOX (especially at 37°C) on the cells viability.

Hence, at the mentioned concentration of free DOX, the average percentages of SKOV-3 cells viability were 85.97 ± 10 % and 72.9 ± 9.1 % at 37°C and 41°C respectively. When the DOX was released from the NPs, even the concentration was very lower, up to 0.07 $\mu g.mL^{-1}$, a higher amont of cells death could be achieved. Indeed as depicted in figure 11, for the concentration of 0.02, 0.03, 0.04, 0.05, 0.07 $\mu g.mL^{-1}$, the cells viability at 37°C was of 94.6 ± 6.1 %, 88.5 ± 0.9 %, 78.9 ± 6.1 %, 71.3 ± 0.8 %, 66.0 ± 5.1 % respectively. At 41°C, the combination of the DOX release and the increase of the temperature

led to the increase of the cytotoxicity towards the cancer cells. As shown in Figure 11, for the same DOX concentration as mentioned before, the cells viability was of 95.0 ± 15.7 %, 80.78 ± 6.1 %, 58.8 ± 9.1 %, 48.0 ± 6.9 %, 32.9 ± 4.3 % respectively. A cell death of almost 70% can then be reached for for a DOX concentration as low as 0.07µg.mL^{-1}, which demonstrate the higher impact of the coated MNPs on the cancer cells. Those systems can then be promising candidates for new tools for cancer therapy.

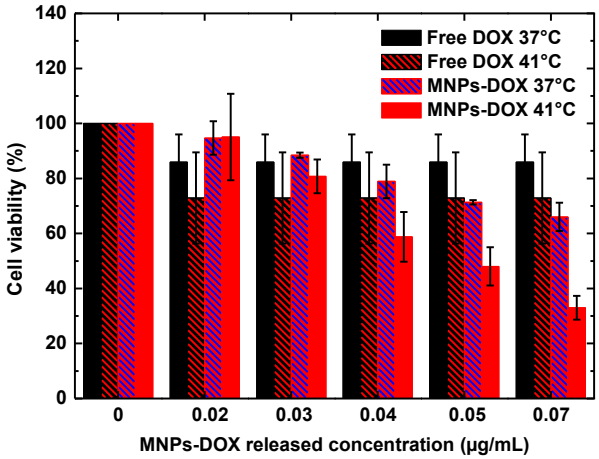


Figure 11. Viability of SKOV3 cells after 24 h exposure to free DOX, $Fe_{3-\delta}O_4$@P(MEO_2MA_{60}-$OEGMA_{40}$) and $Fe_{3-\delta}O_4$@P(MEO_2MA_{60}-$OEGMA_{40}$)-DOX MNPs at 37 or 41°C.

CONCLUSIONS

Core/shell $Fe_{3-\delta}O_4$@P(MEO_2MA_X-$OEGMA_{100-X}$) MNPs were synthesized via SI-ARGET ATRP by growing the poly(MEO_2MA_X-$OEGMA_{100-X}$) copolymers from the surface of $Fe_{3-\delta}O_4$ MNPs. These core/shell MNPs exhibit a thermo-responsive behavior that could be controlled by tuning the molar ratio of MEO_2MA and OEGMA monomers. The magnetic hyperthermia properties of the MNPs was higlighted. The thermo-responsive behavior denoted by a LCST showed lower values in DMEM. The cytotoxic tests towards human ovary cancer cells SKOV-3 showed that the core/shell MNPs had almost no toxicity at concentrations up to 12 µg.mL^{-1}, while when loaded with DOX, a cytotoxic effect and a decrease of SKOV-3 cell viability in a short time and at very low concentration of DOX, as low as 0.07µg.mL^{-1} were observed. This work is a promising way for the design of new tools towards cancer therapy and theragnostic.

ACKNOWLEDGEMENTS

The financial support was given by the Centre National de la Recherche Scientifique (CNRS). French "Ligue Nationale contre le Cancer (CCIR-GE") and the JCS "Center for International Programs", Kazakhstan. The authors would like to thank Jaafar Ghanbaja and the CC MEM of IJL facilities for the TEM and HR-TEM experiments.

REFERENCES

(1) Janko, C.; Ratschker, T.; Nguyen, K.; Zschiesche, L.; Tietze, R.; Lyer, S.; Alexiou, C. Functionalized Superparamagnetic Iron Oxide Nanoparticles (SPIONs) as Platform for the Targeted Multimodal Tumor Therapy. *Front. Oncol.* **2019**, *9*. https://doi.org/10.3389/fonc.2019.00059.
(2) Kandasamy, G.; Maity, D. Recent Advances in Superparamagnetic Iron Oxide Nanoparticles (SPIONs) for in Vitro and in Vivo Cancer Nanotheranostics. *Int. J. Pharm.* **2015**, *496* (2), 191–218. https://doi.org/10.1016/j.ijpharm.2015.10.058.
(3) Cazares-Cortes, E.; Espinosa, A.; Guigner, J.-M.; Michel, A.; Griffete, N.; Wilhelm, C.; Ménager, C. Doxorubicin Intracellular Remote Release from Biocompatible Oligo(Ethylene Glycol) Methyl Ether Methacrylate-Based Magnetic Nanogels Triggered by Magnetic Hyperthermia. *ACS Appl. Mater. Interfaces* **2017**, *9* (31), 25775–25788. https://doi.org/10.1021/acsami.7b06553.
(4) Mertz, D.; Sandre, O.; Bégin-Colin, S. Drug Releasing Nanoplatforms Activated by Alternating Magnetic Fields. *Biochim. Biophys. Acta BBA - Gen. Subj.* **2017**, *1861* (6), 1617–1641. https://doi.org/10.1016/j.bbagen.2017.02.025.
(5) Thirunavukkarasu, G. K.; Cherukula, K.; Lee, H.; Jeong, Y. Y.; Park, I.-K.; Lee, J. Y. Magnetic Field-Inducible Drug-Eluting Nanoparticles for Image-Guided Thermo-Chemotherapy. *Biomaterials* **2018**, *180*, 240–252. https://doi.org/10.1016/j.biomaterials.2018.07.028.
(6) Xue, W.; Liu, X.-L.; Ma, H.; Xie, W.; Huang, S.; Wen, H.; Jing, G.; Zhao, L.; Liang, X.-J.; Fan, H. M. AMF Responsive DOX-Loaded Magnetic Microspheres: Transmembrane Drug Release Mechanism and Multimodality Postsurgical Treatment of Breast Cancer. *J. Mater. Chem. B* **2018**, *6* (15), 2289–2303. https://doi.org/10.1039/C7TB03206D.
(7) Périgo, E. A.; Hemery, G.; Sandre, O.; Ortega, D.; Garaio, E.; Plazaola, F.; Teran, F. J. Fundamentals and Advances in Magnetic Hyperthermia. *Appl. Phys. Rev.* **2015**, *2* (4), 041302. https://doi.org/10.1063/1.4935688.
(8) Annamaneni, S.; Vishwakarma, S. K.; Meka, P. B.; Khan, A. A.; Nallari, P. Regulation of Heat Shock Protein-70 Gene Transcripts in Breast Cancer Cells during Hypo and Hyperthermia Exposure. *Meta Gene* **2019**, *20*, 100548. https://doi.org/10.1016/j.mgene.2019.100548.
(9) Das, P.; Colombo, M.; Prosperi, D. Recent Advances in Magnetic Fluid Hyperthermia for Cancer Therapy. *Colloids Surf. B Biointerfaces* **2019**, *174*, 42–55. https://doi.org/10.1016/j.colsurfb.2018.10.051.
(10) Saliev, T.; Feril, L. B.; Begimbetova, D.; Baiskhanova, D.; Klodzinskyi, A.; Bobrova, X.; Aipov, R.; Baltabayeva, T.; Tachibana, K. Hyperthermia Enhances Bortezomib-Induced Apoptosis in Human White Blood Cancer Cells. *J. Therm. Biol.* **2017**, *67*, 9–14. https://doi.org/10.1016/j.jtherbio.2017.04.009.
(11) Andrä, W.; Nowak, H. *Magnetism in Medicine: A Handbook*; John Wiley & Sons, 2007.
(12) Bañobre-López, M.; Teijeiro, A.; Rivas, J. Magnetic Nanoparticle-Based Hyperthermia for Cancer Treatment. *Rep. Pract. Oncol. Radiother.* **2013**, *18* (6), 397–400. https://doi.org/10.1016/j.rpor.2013.09.011.
(13) Thorat, N. D.; Bohara, R. A.; Noor, M. R.; Dhamecha, D.; Soulimane, T.; Tofail, S. A. M. Effective Cancer Theranostics with Polymer Encapsulated Superparamagnetic Nanoparticles:

Combined Effects of Magnetic Hyperthermia and Controlled Drug Release. *ACS Biomater. Sci. Eng.* **2017**, *3* (7), 1332–1340. https://doi.org/10.1021/acsbiomaterials.6b00420.
(14) Guo, X.; Li, W.; Luo, L.; Wang, Z.; Li, Q.; Kong, F.; Zhang, H.; Yang, J.; Zhu, C.; Du, Y.; et al. External Magnetic Field-Enhanced Chemo-Photothermal Combination Tumor Therapy via Iron Oxide Nanoparticles. *ACS Appl. Mater. Interfaces* **2017**, *9* (19), 16581–16593. https://doi.org/10.1021/acsami.6b16513.
(15) Hervault, A.; Dunn, A. E.; Lim, M.; Boyer, C.; Mott, D.; Maenosono, S.; Thanh, N. T. K. Doxorubicin Loaded Dual PH- and Thermo-Responsive Magnetic Nanocarrier for Combined Magnetic Hyperthermia and Targeted Controlled Drug Delivery Applications. *Nanoscale* **2016**, *8* (24), 12152–12161. https://doi.org/10.1039/C5NR07773G.
(16) Blanco-Andujar, C.; Walter, A.; Cotin, G.; Bordeianu, C.; Mertz, D.; Felder-Flesch, D.; Begin-Colin, S. Design of Iron Oxide-Based Nanoparticles for MRI and Magnetic Hyperthermia. *Nanomed.* **2016**, *11* (14), 1889–1910. https://doi.org/10.2217/nnm-2016-5001.
(17) Lara, S.; Perez-Potti, A.; Herda, L. M.; Adumeau, L.; Dawson, K. A.; Yan, Y. Differential Recognition of Nanoparticle Protein Corona and Modified Low-Density Lipoprotein by Macrophage Receptor with Collagenous Structure. *ACS Nano* **2018**, *12* (5), 4930–4937. https://doi.org/10.1021/acsnano.8b02014.
(18) Zhao, N.; Yan, L.; Zhao, X.; Chen, X.; Li, A.; Zheng, D.; Zhou, X.; Dai, X.; Xu, F.-J. Versatile Types of Organic/Inorganic Nanohybrids: From Strategic Design to Biomedical Applications. *Chem. Rev.* **2019**, *119* (3), 1666–1762. https://doi.org/10.1021/acs.chemrev.8b00401.
(19) Nath, N.; Chilkoti, A. Creating "Smart" Surfaces Using Stimuli Responsive Polymers. *Adv. Mater.* **2002**, *14* (17), 1243–1247. https://doi.org/10.1002/1521-4095(20020903)14:17<1243::AID-ADMA1243>3.0.CO;2-M.
(20) Teotia, A. K.; Sami, H.; Kumar, A. 1 - Thermo-Responsive Polymers: Structure and Design of Smart Materials. In *Switchable and Responsive Surfaces and Materials for Biomedical Applications*; Zhang, Z., Ed.; Woodhead Publishing: Oxford, 2015; pp 3–43. https://doi.org/10.1016/B978-0-85709-713-2.00001-8.
(21) Hoogenboom, R. 2 - Temperature-Responsive Polymers: Properties, Synthesis and Applications. In *Smart Polymers and their Applications*; Aguilar, M. R., San Román, J., Eds.; Woodhead Publishing, 2014; pp 15–44. https://doi.org/10.1533/9780857097026.1.15.
(22) Schmaljohann, D. Thermo- and PH-Responsive Polymers in Drug Delivery. *Adv. Drug Deliv. Rev.* **2006**, *58* (15), 1655–1670. https://doi.org/10.1016/j.addr.2006.09.020.
(23) Roy, D.; Brooks, W. L. A.; Sumerlin, B. S. New Directions in Thermoresponsive Polymers. *Chem. Soc. Rev.* **2013**, *42* (17), 7214–7243. https://doi.org/10.1039/C3CS35499G.
(24) Ferjaoui, Z.; Schneider, R.; Meftah, A.; Gaffet, E.; Alem, H. Functional Responsive Superparamagnetic Core/Shell Nanoparticles and Their Drug Release Properties. *RSC Adv.* **2017**, *7* (42), 26243–26249. https://doi.org/10.1039/C7RA02437A.
(25) Jamal Al Dine, E.; Ferjaoui, Z.; Ghanbaja, J.; Roques-Carmes, T.; Meftah, A.; Hamieh, T.; Toufaily, J.; Schneider, R.; Marchal, S.; Gaffet, E.; et al. Thermo-Responsive Magnetic Fe3O4@P(MEO2MAX-OEGMA100-X) NPs and Their Applications as Drug Delivery Systems. *Int. J. Pharm.* **2017**, *532* (2), 738–747. https://doi.org/10.1016/j.ijpharm.2017.09.019.
(26) Dine, E. J. A.; Ferjaoui, Z.; Roques-Carmes, T.; Schjen, A.; Meftah, A.; Tayssir Hamieh; Toufaily, J.; Schneider, R.; Gaffet, E.; Alem, H. Efficient Synthetic Access to Thermo-Responsive Core/Shell Nanoparticles. *Nanotechnology* **2017**, *28* (12), 125601. https://doi.org/10.1088/1361-6528/aa5d81.
(27) Plunkett, K. N.; Zhu, X.; Moore, J. S.; Leckband, D. E. PNIPAM Chain Collapse Depends on the Molecular Weight and Grafting Density. *Langmuir* **2006**, *22* (9), 4259–4266. https://doi.org/10.1021/la0531502.
(28) Vihola, H.; Laukkanen, A.; Valtola, L.; Tenhu, H.; Hirvonen, J. Cytotoxicity of Thermosensitive Polymers Poly(N-Isopropylacrylamide), Poly(N-Vinylcaprolactam) and

Amphiphilically Modified Poly(N-Vinylcaprolactam). *Biomaterials* **2005**, *26* (16), 3055–3064. https://doi.org/10.1016/j.biomaterials.2004.09.008.
(29) Li, L.; Zhang, C.; Zhang, R.; Xu, Z.; Xu, Z.; Whittaker, A. K. Multifunctional Magnetized Porous Silica Covered with Poly(2-Dimethylaminoethyl Methacrylate) for PH Controllable Drug Release and Magnetic Resonance Imaging. *ACS Appl. Nano Mater.* **2018**, *1* (9), 5027–5034. https://doi.org/10.1021/acsanm.8b01131.
(30) Macchione, M. A.; Biglione, C.; Strumia, M. Design, Synthesis and Architectures of Hybrid Nanomaterials for Therapy and Diagnosis Applications. *Polymers* **2018**, *10* (5), 527. https://doi.org/10.3390/polym10050527.
(31) Shim, M. S.; Kwon, Y. J. Stimuli-Responsive Polymers and Nanomaterials for Gene Delivery and Imaging Applications. *Adv. Drug Deliv. Rev.* **2012**, *64* (11), 1046–1059. https://doi.org/10.1016/j.addr.2012.01.018.
(32) Priya James, H.; John, R.; Alex, A.; Anoop, K. R. Smart Polymers for the Controlled Delivery of Drugs – a Concise Overview. *Acta Pharm. Sin. B* **2014**, *4* (2), 120–127. https://doi.org/10.1016/j.apsb.2014.02.005.
(33) Mortensen, N. P.; Hurst, G. B.; Wang, W.; Foster, C. M.; Nallathamby, P. D.; Retterer, S. T. Dynamic Development of the Protein Corona on Silica Nanoparticles: Composition and Role in Toxicity. *Nanoscale* **2013**, *5* (14), 6372–6380. https://doi.org/10.1039/C3NR33280B.
(34) García-Álvarez, R.; Hadjidemetriou, M.; Sánchez-Iglesias, A.; Liz-Marzán, L. M.; Kostarelos, K. In Vivo Formation of Protein Corona on Gold Nanoparticles. The Effect of Their Size and Shape. *Nanoscale* **2018**, *10* (3), 1256–1264. https://doi.org/10.1039/C7NR08322J.
(35) Al-Ahmady, Z. S.; Hadjidemetriou, M.; Gubbins, J.; Kostarelos, K. Formation of Protein Corona in Vivo Affects Drug Release from Temperature-Sensitive Liposomes. *J. Controlled Release* **2018**, *276*, 157–167. https://doi.org/10.1016/j.jconrel.2018.02.038.
(36) Caracciolo, G.; Farokhzad, O. C.; Mahmoudi, M. Biological Identity of Nanoparticles In Vivo: Clinical Implications of the Protein Corona. *Trends Biotechnol.* **2017**, *35* (3), 257–264. https://doi.org/10.1016/j.tibtech.2016.08.011.
(37) Tenzer, S.; Docter, D.; Kuharev, J.; Musyanovych, A.; Fetz, V.; Hecht, R.; Schlenk, F.; Fischer, D.; Kiouptsi, K.; Reinhardt, C.; et al. Rapid Formation of Plasma Protein Corona Critically Affects Nanoparticle Pathophysiology. *Nat. Nanotechnol.* **2013**, *8* (10), 772–781. https://doi.org/10.1038/nnano.2013.181.
(38) Corbo, C.; Molinaro, R.; Tabatabaei, M.; Farokhzad, O. C.; Mahmoudi, M. Personalized Protein Corona on Nanoparticles and Its Clinical Implications. *Biomater. Sci.* **2017**, *5* (3), 378–387. https://doi.org/10.1039/C6BM00921B.
(39) Gillich, T.; Acikgöz, C.; Isa, L.; Schlüter, A. D.; Spencer, N. D.; Textor, M. PEG-Stabilized Core–Shell Nanoparticles: Impact of Linear versus Dendritic Polymer Shell Architecture on Colloidal Properties and the Reversibility of Temperature-Induced Aggregation. *ACS Nano* **2013**, *7* (1), 316–329. https://doi.org/10.1021/nn304045q.
(40) Sun, Q.; Cheng, D.; Yu, X.; Zhang, Z.; Dai, J.; Li, H.; Liang, B.; Shuai, X. A PH-Sensitive Polymeric Nanovesicle Based on Biodegradable Poly(Ethylene Glycol)-b-Poly(2-(Diisopropylamino)Ethyl Aspartate) as a MRI-Visible Drug Delivery System. *J. Mater. Chem.* **2011**, *21* (39), 15316–15326. https://doi.org/10.1039/C1JM12404H.
(41) Lutz, J.-F. Polymerization of Oligo(Ethylene Glycol) (Meth)Acrylates: Toward New Generations of Smart Biocompatible Materials. *J. Polym. Sci. Part Polym. Chem.* **2008**, *46* (11), 3459–3470. https://doi.org/10.1002/pola.22706.
(42) Gao, X.; Kučerka, N.; Nieh, M.-P.; Katsaras, J.; Zhu, S.; Brash, J. L.; Sheardown, H. Chain Conformation of a New Class of PEG-Based Thermoresponsive Polymer Brushes Grafted on Silicon as Determined by Neutron Reflectometry. *Langmuir* **2009**, *25* (17), 10271–10278. https://doi.org/10.1021/la901086e.
(43) Alem, H.; Schejn, A.; Roques-Carmes, T.; Ghanbaja, J.; Schneider, R. Thermo-Responsive

and Aqueous Dispersible ZnO/PNIPAM Core/Shell Nanoparticles. *Nanotechnology* **2015**, *26* (33), 335605. https://doi.org/10.1088/0957-4484/26/33/335605.
(44) Martínez-López, J. F.; Schneider, S.; Salavera, D.; Mainar, A. M.; Urieta, J. S.; Pardo, J. I. Molar Heat Capacities of the Mixture {1,8-Cineole+ethanol} at Several Temperatures and Atmospheric Pressure. *J. Chem. Thermodyn.* **2016**, *92*, 146–151. https://doi.org/10.1016/j.jct.2015.09.012.
(45) Abumandour, E.-S.; Mutelet, F.; Alonso, D. Performance of an Absorption Heat Transformer Using New Working Binary Systems Composed of {ionic Liquid and Water}. *Appl. Therm. Eng.* **2016**, *94*, 579–589. https://doi.org/10.1016/j.applthermaleng.2015.10.107.
(46) Daou, T. J.; Pourroy, G.; Bégin-Colin, S.; Grenèche, J. M.; Ulhaq-Bouillet, C.; Legaré, P.; Bernhardt, P.; Leuvrey, C.; Rogez, G. Hydrothermal Synthesis of Monodisperse Magnetite Nanoparticles. *Chem. Mater.* **2006**, *18* (18), 4399–4404. https://doi.org/10.1021/cm060805r.
(47) Baaziz, W.; Pichon, B. P.; Fleutot, S.; Liu, Y.; Lefevre, C.; Greneche, J.-M.; Toumi, M.; Mhiri, T.; Begin-Colin, S. Magnetic Iron Oxide Nanoparticles: Reproducible Tuning of the Size and Nanosized-Dependent Composition, Defects, and Spin Canting. *J. Phys. Chem. C* **2014**, *118* (7), 3795–3810. https://doi.org/10.1021/jp411481p.
(48) GUO, Y.; LIU, H.-J.; CHEN, J.-Q.; SHANG, Y.-Z.; LIU, H.-L. Synthesis of P(MEO2MA-co-OEGMA) Random Copolymers and Thermally Induced Phase Transition Behaviors in Aqueous Solutions https://www.ingentaconnect.com/content/apcs/apcs/2015/00000031/00000010/art00010 (accessed Sep 27, 2018). https://doi.org/info:doi/10.3866/PKU.WHXB201508263.
(49) Colthup, N. B.; Daly, L. H.; Wiberley, S. E. *Introduction to Infrared and Raman Spectroscopy*; Academic Press, 1964.
(50) Vigevani, A.; Ballabio, M.; Gandini, E.; Penco, S. 1H NMR and IR Spectra of Antitumour Anthracyclines: Effect of the Substitution Pattern on the Chemical Shift Values of the Phenolic Protons and on IR Absorptions of the Quinone System. *Magn. Reson. Chem.* **1985**, *23* (5), 344–352. https://doi.org/10.1002/mrc.1260230513.
(51) Guo, L.; Ding, W. Immobilized Transferrin Fe3O4@SiO2 Nanoparticle with High Doxorubicin Loading for Dual-Targeted Tumor Drug Delivery. *Int. J. Nanomedicine* **2013**, 4631. https://doi.org/10.2147/IJN.S51745.
(52) Mura, S.; Nicolas, J.; Couvreur, P. Stimuli-Responsive Nanocarriers for Drug Delivery. *Nat. Mater.* **2013**, *12* (11), 991–1003. https://doi.org/10.1038/nmat3776.